Nuclear Science and Techniques (2023) 34:94
https://doi.org/10.1007/s41365-023-01241-z

Probing nucleon effective mass splitting with light particle emission

Fang-Yuan Wang[1] · Jun-Ping Yang[1] · Xiang Chen[1] · Ying Cui[1] · Yong-Jia Wang[2] · Zhi-Gang Xiao[3] · Zhu-Xia Li[1] · Ying-Xun Zhang[1,4]

Received: 9 April 2023 / Revised: 26 April 2023 / Accepted: 26 April 2023 / Published online: 26 June 2023
© The Author(s), under exclusive licence to China Science Publishing & Media Ltd. (Science Press), Shanghai Institute of Applied Physics, the Chinese Academy of Sciences, Chinese Nuclear Society 2023

Abstract
The main objective of this study was to investigate the impact of effective mass splitting on heavy-ion-collision observables. We first analyzed correlations between different nuclear matter parameters obtained from 119 effective Skyrme interaction sets. The values of the correlation coefficients illustrate that the magnitude of effective mass splitting is crucial for tight constraints on the symmetry energy via heavy-ion collisions. The ^{86}Kr + ^{208}Pb system at beam energies ranging from 25 to 200A MeV was simulated within the framework of the improved quantum molecular dynamics model (ImQMD-Sky). Our calculations show that the slopes of the spectra of $\ln[Y(\mathrm{n})/Y(\mathrm{p})]$ and $\ln[Y(\mathrm{t})/Y(^3\mathrm{He})]$, which are the logarithms of the neutron to proton and triton to helium-3 yield ratios, are directly related to effective mass splitting and can be used to probe the effective mass splitting.

Keywords Effective mass splitting · Symmetry energy · Heavy-ion collisions · Skyrme interaction

1 Introduction

The nucleon effective mass m^*_N is used to describe the motion of nucleons in a momentum-dependent potential, which is equivalent to the motion of a quasi-nucleon of mass m^*_N in a momentum-independent potential [1–4]. Isospin splitting of the nucleon effective mass indicates that the neutron effective mass is not equal to the proton effective mass, that is, $m^*_\mathrm{n} \neq m^*_\mathrm{p}$, in isospin asymmetric nuclear matter. Both the effective mass and effective mass splitting are important quantities in the isospin asymmetric nuclear equation of state and serve as important microscopic inputs for the study of the thermal properties of protoneutron stars, such as thermal conductivity [5, 6], specific heat [7], and neutrino reaction rates [8–12]. Furthermore, effective mass splitting is important for improving symmetry energy constraints [13].

Much effort has been made to constrain effective mass splitting using heavy-ion collisions (HICs) [13–18], nucleon–nucleus optical potentials [19–21], and giant monopole resonance [22–25]. An interesting finding is that the effective mass splitting obtained using the nucleon–nucleus optical potential analysis favors $m^*_\mathrm{n} > m^*_\mathrm{p}$ [19], whereas the HIC data support $m^*_\mathrm{n} < m^*_\mathrm{p}$ [13–15, 17, 26]. A possible reason for this discrepancy is that the different probes reflect values of the effective mass splitting at different densities and momentum regions. Further understanding of the constraints of effective mass splitting by HICs requires new probes for neutron-rich HICs and comparison with experimental observables in the future.

Currently, the new generation rare isotope facilities or planned facilities, such as the Heavy Ion Research Facility in Lanzhou (HIRFL/Lanzhou) [27], Facility for Rare Isotope Beams at Michigan State University (FRIB/MSU) [28], Radioactive Isotope Beam Factory (RIBF/RIKEN)

This work was supported by the National Natural Science Foundation of China (Nos. 12275359, 11875323, 11961141003, U2032145, and 11890712), the National Key R &D Program of China (No. 2018YFA0404404), the Continuous Basic Scientific Research Project (Nos. WDJC-2019-13 and BJ20002501), and funding from the China Institute of Atomic Energy (No. YZ222407001301) .

✉ Ying-Xun Zhang
zhyx@ciae.ac.cn

[1] China Institute of Atomic Energy, Beijing 102413, China

[2] School of Science, Huzhou University, Huzhou 313000, China

[3] Department of Physics, Tsinghua University, Beijing 100084, China

[4] Guangxi Key Laboratory of Nuclear Physics and Technology, Guangxi Normal University, Guilin 541004, China

[29], Rare isotope Accelerator complex for ON-line experiment (RAON/Korea) [30], and Beijing Isotope Separation On-line (BISOL/Beijing) [31], can produce rare isotope beams from tens to hundreds MeV per nucleon for studying the dynamical evolution of neutron-rich nuclear systems. Some important neutron-rich HIC experiments [32–36] have been performed to extract information on the density dependence of symmetry energy and effective mass splitting by comparing the data with transport model simulations [34, 37].

Recently, an experiment on the ^{86}Kr + ^{208}Pb system was performed using the Compact Spectrometer for Heavy IoN Experiment (CSHINE) [38–41], which was installed at the final focal plane of the Radioactive Ion Beam Line in Lanzhou (RIBLL-I/HIRFL) [42, 43]. Both yield and kinetic variables of the $A = 3$ isobars, that is, t and ^{3}He, were measured. This provides an opportunity to constrain the symmetry energy [44] at subsaturation densities and further verify the capability of the transport models. In addition, constraining effective mass splitting using the facilities in Lanzhou requires calculations to extend the beam energy of ∼100A–200A MeV, as this energy region has been found to be the optimal beam energy in previous calculations [13, 45].

In this study, we first analyze the correlations between different nuclear matter parameters to illustrate the significance of the investigation of effective mass splitting. We then investigate the impacts of effective mass splitting on the HIC observables, such as neutron to proton yield ratios, triton to helium-3 yield ratios, of the ^{86}Kr + ^{208}Pb system at beam energies ranging from 25A to 200A MeV using ImQMD-Sky model.

2 Theoretical model

In the ImQMD-Sky model, each nucleon is represented by a Gaussian wave packet given by

$$\phi_{k_{i0}}(\boldsymbol{r}_i) = \frac{1}{(2\pi\sigma_r^2)^{3/4}} \exp\left[-\frac{(\boldsymbol{r}_i-\boldsymbol{r}_{i0})^2}{4\sigma_r^2} + \mathrm{i}(\boldsymbol{r}_i-\boldsymbol{r}_{i0})\cdot\boldsymbol{k}_{i0}\right], \tag{1}$$

where σ_r and $\boldsymbol{r}_{i0}$ denote the width and centroid of the wave packet, respectively; $\boldsymbol{k}_{i0}$ is the momentum of the nucleon; and the subscript k_{i0} corresponds to the state of the ith nucleon. For an N-body system, the system wavefunction is assumed to be a direct product of N coherent states:

$$\Psi(\boldsymbol{r}_1,\ldots,\boldsymbol{r}_N) = \phi_{k_1}(\boldsymbol{r}_1)\phi_{k_2}(\boldsymbol{r}_2)\ldots\phi_{k_N}(\boldsymbol{r}_N). \tag{2}$$

By using the Wigner transformation, the phase-space density distribution of the system can be obtained as

$$\begin{aligned} &f_N(\boldsymbol{r}_1,\ldots,\boldsymbol{r}_N;\boldsymbol{p}_1,\ldots,\boldsymbol{p}_N)\\ &\quad= \Pi_i \frac{1}{(\pi\hbar)^3} \exp\left[-\frac{(\boldsymbol{r}_i-\boldsymbol{r}_{i0})^2}{2\sigma_r^2} - \frac{(\boldsymbol{p}_i-\boldsymbol{p}_{i0})^2}{2\sigma_p^2}\right], \end{aligned} \tag{3}$$

where $\sigma_r\sigma_p = \hbar/2$ and $\boldsymbol{r}_i$ and $\boldsymbol{p}_i$ denote the position and momentum of the ith nucleon, respectively. The Hamiltonian of the nucleonic part is calculated as follows:

$$\begin{aligned} H &= \langle\Psi|\hat{T}+\hat{U}|\Psi\rangle\\ &\equiv \sum_i \int \frac{\hat{\boldsymbol{p}}_i^2}{2m} f_i(\boldsymbol{r},\boldsymbol{p})\mathrm{d}^3r\mathrm{d}^3p\\ &\quad+ \sum_{i<j} \int \hat{v}^{ij}_{sky} f_i(\boldsymbol{r},\boldsymbol{p}) f_j(\boldsymbol{r}',\boldsymbol{p}')\mathrm{d}^3r\mathrm{d}^3p\mathrm{d}^3r'\mathrm{d}^3p'\\ &= \sum_i \left(\frac{p_{i0}^2}{2m} + C(\sigma_r)\right) + \int u_{\mathrm{sky}}\mathrm{d}^3r. \end{aligned} \tag{4}$$

Where $C(\sigma_r) = \frac{1}{2m}\frac{3\hbar^2}{4\sigma_r^2}$ denotes the contribution of the wave packet width to the kinetic energy term and u_{sky} is the potential energy density in coordinate space.

For the nucleonic potential, the Skyrme-type nucleonic potential energy density without the spin-orbit term is used:

$$u_{\mathrm{sky}} = u_{\mathrm{loc}} + u_{\mathrm{md}}. \tag{5}$$

The local potential energy density is

$$\begin{aligned} u_{\mathrm{loc}} &= \frac{\alpha}{2}\frac{\rho^2}{\rho_0} + \frac{\beta}{\eta+1}\frac{\rho^{\eta+1}}{\rho_0^{\eta}} + \frac{g_{\mathrm{sur}}}{2\rho_0}(\nabla\rho)^2\\ &\quad+ \frac{g_{\mathrm{sur,iso}}}{\rho_0}[\nabla(\rho_{\mathrm{n}}-\rho_{\mathrm{p}})]^2\\ &\quad+ A_{\mathrm{sym}}\frac{\rho^2}{\rho_0}\delta^2 + B_{\mathrm{sym}}\frac{\rho^{\eta+1}}{\rho_0^{\eta}}\delta^2, \end{aligned} \tag{6}$$

where $\rho = \rho_{\mathrm{n}} + \rho_{\mathrm{p}}$ is the nucleon density, $\delta = (\rho_{\mathrm{n}} - \rho_{\mathrm{p}})/\rho$ is the isospin asymmetry, α is a parameter related to the two-body term, β and η are related to the three-body term, g_{sur} and $g_{\mathrm{sur,iso}}$ are related to the surface terms, and A_{sym} and B_{sym} are the coefficients of the symmetry potential that originate from the two- and three-body interaction terms [46]. Their values can be obtained from the standard Skyrme interactions.

The nonlocal potential energy density or momentum-dependent interaction term, that is, u_{md}, is also considered as a Skyrme-type momentum-dependent energy density functional. It is obtained based on its interaction form $\delta(\boldsymbol{r}_1-\boldsymbol{r}_2)(\boldsymbol{p}_1-\boldsymbol{p}_2)^2$ [47], that is,

$$
\begin{aligned}
u_{\mathrm{md}} = C_0 \sum_{ij} \int \mathrm{d}^3p\mathrm{d}^3p' f_i(\boldsymbol{r},\boldsymbol{p}) f_j(\boldsymbol{r},\boldsymbol{p}')(\boldsymbol{p}-\boldsymbol{p}')^2 \\
+ D_0 \sum_{ij\in n} \int \mathrm{d}^3p\mathrm{d}^3p' f_i(\boldsymbol{r},\boldsymbol{p}) f_j(\boldsymbol{r},\boldsymbol{p}')(\boldsymbol{p}-\boldsymbol{p}')^2 \\
+ D_0 \sum_{ij\in p} \int \mathrm{d}^3p\mathrm{d}^3p' f_i(\boldsymbol{r},\boldsymbol{p}) f_j(\boldsymbol{r},\boldsymbol{p}')(\boldsymbol{p}-\boldsymbol{p}')^2,
\end{aligned}
\tag{7}
$$

where C_0 and D_0 are parameters related to momentum-dependent interactions. These are related to the standard Skyrme interaction as follows:

$$
\begin{aligned}
C_0 &= \frac{1}{16\hbar^2}\left[t_1(2+x_1)+t_2(2+x_2)\right] \\
D_0 &= \frac{1}{16\hbar^2}\left[t_2(2x_2+1)-t_1(2x_1+1)\right].
\end{aligned}
\tag{8}
$$

Further details can be found in Ref. [48]. The parameters in Eqs. (6) and (7) are obtained from the standard Skyrme interaction parameters as in Refs. [49, 50]. The Coulomb term was treated using the standard method in quantum molecular dynamics type models.

Initialization was performed in the same manner as in Ref. [46]. The centroids of the wave packets for neutrons and protons were sampled within the empirical radii of neutrons and protons [46]. After the positions of all nucleons are finally prepared, the density distribution is known. The momenta of nucleons were sampled using a local density approach.

It should be noted that the effects of the width of the wave packet on the momentum sampling in the initialization are considered in this work. Usually, $C(\sigma_r)$ is omitted in the quantum molecular dynamics type models for the study of intermediate-high energy HICs because it has no effect on the equation of motion, and its correction to the initial momentum is relatively small. However, this effect cannot be neglected, particularly when studying low-energy reactions. This is because $C(\sigma_r)$ in the kinetic energy term reaches ~25% of the Fermi energy at a normal density, ~35 MeV. For example, $C(\sigma_r)$ is 8.97 MeV when the width of the wave packet takes a typical value, that is, $\sigma_r = 1.32$ fm. For the expected momentum values of the nucleons sampled in the calculations, the width of the wave packet has no direct effect because $\langle\phi_i|\boldsymbol{p}|\phi_i\rangle = \boldsymbol{p}_{i0}$. To satisfy the requirements for reasonably describing the binding energy of the initial nuclei with Gaussian wave packets [51–53], the sampled $\boldsymbol{p}_{i0}$ should be reduced to a smaller value than that obtained without considering the width of the wave packet.

3 Results and discussion

To understand the importance of effective mass splitting on symmetry energy constraints, we first analyzed the correlations between different nuclear matter parameters. Subsequently, the influence of effective mass splitting on the HIC observables is presented and discussed.

3.1 Nuclear matter parameters and their correlations

For the Skyrme effective interaction used in this work, the corresponding isospin asymmetric equation of state for cold nuclear matter is

$$
\begin{aligned}
E/A = \frac{3\hbar^2}{10m}\left(\frac{3\pi^2}{2}\rho\right)^{2/3} \\
+ \frac{\alpha}{2}\frac{\rho}{\rho_0} + \frac{\beta}{\eta+1}\frac{\rho^\eta}{\rho_0^\eta} + g_{\rho\tau}\frac{\rho^{5/3}}{\rho_0^{5/3}} + S(\rho)\delta^2,
\end{aligned}
\tag{9}
$$

where the density dependence of the symmetry energy $S(\rho)$ is

$$
\begin{aligned}
S(\rho) = \frac{\hbar^2}{6m}\left(\frac{3\pi^2\rho}{2}\right)^{2/3} + A_{\mathrm{sym}}\frac{\rho}{\rho_0} \\
+ B_{\mathrm{sym}}\left(\frac{\rho}{\rho_0}\right)^\eta + C_{\mathrm{sym}}(m_s^*, m_v^*)\left(\frac{\rho}{\rho_0}\right)^{5/3}.
\end{aligned}
\tag{10}
$$

The terms $g_{\rho\tau}$ in Eqs. (9) and C_{sym} in Eq. (10) originate from the energy density functional of the Skyrme-type momentum-dependent interaction, and its relationship to the standard Skyrme interaction can be found in Ref. [54]. The pressure in the nuclear fluid is calculated as follows:

$$
P = \rho^2\frac{\partial E/A(\rho,\delta)}{\partial\rho}.
\tag{11}
$$

The saturation density ρ_0 for symmetric nuclear matter is obtained using

$$
P = \rho_0^2\left(\frac{\mathrm{d}}{\mathrm{d}\rho}\frac{E}{A}(\rho,\delta=0)\right)|_{\rho=\rho_0} = 0.
\tag{12}
$$

Correspondingly, the nuclear matter parameters at the saturation density were obtained. For example, the binding energy E_0 and the incompressibility K_0 are

$$
E_0 = E/A(\rho_0),
\tag{13}
$$

$$
K_0 = 9\rho_0^2\frac{\partial^2 E/A}{\partial\rho^2}|_{\rho_0}.
\tag{14}
$$

The symmetry energy coefficient S_0 and slope of the symmetry energy L are

$$
S_0 = S(\rho_0),
\tag{15}
$$

$$L = 3\rho_0 \frac{\partial S(\rho)}{\partial \rho}|_{\rho_0}. \tag{16}$$

The effective mass of neutron and proton is obtained from the neutron and proton potentials, respectively, as follows:

$$\frac{m}{m_q^*} = 1 + \frac{m}{p}\frac{\partial V_q}{\partial p}, \quad q = \text{n,p}, \tag{17}$$

where V_q is the single-particle potential for a neutron or proton and the form of V_q can be found in Appendix A. For the Skyrme interaction, the neutron and proton effective masses are

$$\frac{m}{m_q^*} = 1 + 4mC_0\rho + 4mD_0\rho_q. \tag{18}$$

The isoscalar effective mass m_s^* can be obtained at $\rho_q = \rho/2$ from Eq. (18), and the isovector effective mass m_v^* can be obtained at $\rho_q = 0$, which represents the neutron (proton) effective mass in pure proton (neutron) matter, as in Refs. [22, 55]. They are

$$\frac{m}{m_s^*} = 1 + 4m\left(C_0 + \frac{D_0}{2}\right)\rho, \tag{19}$$

$$\frac{m}{m_v^*} = 1 + 4mC_0\rho. \tag{20}$$

By using m_s^* and m_v^*, the effective mass splitting $\Delta m_{\text{np}}^* = (m_\text{n}^* - m_\text{p}^*)/m$ can be expressed as

$$\Delta m_{\text{np}}^* = \frac{m_\text{n}^* - m_\text{p}^*}{m} = 2\frac{m_s^*}{m}\sum_{n=1}^{\infty}\left(\frac{m_s^* - m_v^*}{m_v^*}\right)^{2n-1}\delta^{2n-1}, \tag{21}$$

as in Ref. [22]. As described in Eq. (21), the exact value of $\Delta m_{\text{np}}^* = (m_\text{n}^* - m_\text{p}^*)/m$ depends on the expansion and the isospin asymmetry of the system, δ. To avoid dependence on the expansion and δ, we define the quantity

$$f_I = \frac{1}{2\delta}\left(\frac{m}{m_\text{n}^*} - \frac{m}{m_\text{p}^*}\right) = \frac{m}{m_s^*} - \frac{m}{m_v^*} \tag{22}$$

to describe the isospin effective mass splitting, which has the opposite sign to Δm_{np}^*.

Because the aforementioned nuclear matter parameters are obtained from the same energy density functional, one can expect correlations between them. For example, as expressed in Eq. (10), $S(\rho)$ depends on the two-body, three-body, and momentum-dependent interaction terms. These three terms are correlated with E_0, K_0, and m_s^* [55] and S_0, L, and m_v^* [50]. The correlation strength depends on the effective set of Skyrme interaction parameters used [55].

To describe the correlation between different nuclear matter parameters with less bias, one can calculate the linear correlation coefficient C_{AB} between the nuclear matter parameters A and B from the published parameter sets, which satisfy the current knowledge of the nuclear matter parameters [50]:

$$\begin{aligned} 200\text{ MeV} &\leqslant K_0 \leqslant 280\text{ MeV},\\ 25\text{ MeV} &\leqslant S_0 \leqslant 35\text{ MeV},\\ 30\text{ MeV} &\leqslant L \leqslant 120\text{ MeV},\\ 0.6 &\leqslant m_s^*/m \leqslant 1.0,\\ -0.5 &\leqslant f_I \leqslant 0.4. \end{aligned} \tag{23}$$

The quantities A or $B = \{\rho_0, E_0, K_0, S_0, L, m_s^*, m_v^*\}$ and the correlation coefficient C_{AB} are calculated as follows:

$$\begin{aligned} C_{AB} &= \frac{\text{cov}(A,B)}{\sigma(A)\sigma(B)},\\ \text{cov}(A,B) &= \frac{1}{N-1}\sum_i (A_i - \langle A\rangle)(B_i - \langle B\rangle),\\ \sigma(X) &= \sqrt{\frac{1}{N-1}\sum_i (X_i - \langle X\rangle)^2}, \quad X = A, B\\ \langle X\rangle &= \frac{1}{N}\sum_i X_i, \quad i = 1, \ldots, N, \end{aligned} \tag{24}$$

where $\text{cov}(A,B)$ is the covariance between A and B, $\sigma(X)$ is the standard deviation of X, and $\langle X\rangle$ denotes the average values obtained from $N = 119$ standard Skyrme parameter sets, selected according to the criteria in Eq. (23).

The values of these parameters are listed in Table 1, and the correlation coefficients C_{AB} are shown in Fig. 1. A positive value of C_{AB} reflects a positive linear correlation, whereas a negative value indicates a negative linear correlation. Correlations exist between the different nuclear matter parameters. Specifically, the correlations between S_0 and ρ_0, L and S_0, m_v^* and m_s^*, K_0 and ρ_0, and S_0 and E_0 are stronger than those of the other nuclear matter parameter pairs. The 'strange' correlation between ρ_0 and S_0 can be understood as follows: ρ_0 can be determined using Eq. (12), which is related to the parameters α, β, η, and $g_{\rho\tau}$, or to the nuclear matter parameters, as presented in Eq. (5) of Ref. [50]. These correlations indicate that obtaining tight constraints on the density dependence of the symmetry energy using HICs requires knowing information not only on S_0 and L but also on m_s^* and m_v^* (or the effective mass splitting).

3.2 Symmetry potential

Based on Eq. (17), effective mass splitting is related to the symmetry potential, which plays an important role in HICs. The symmetry potential V_{sym} is also called the Lane

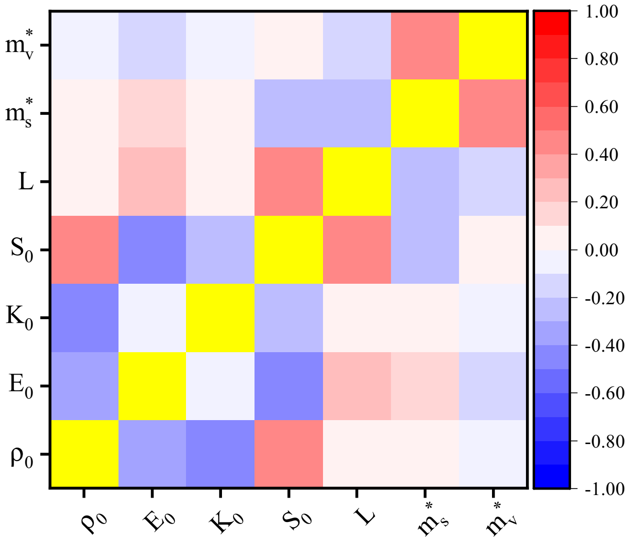

Fig. 1 (Color online) Correlation coefficients between the different nuclear matter parameter pairs

potential, which equals the difference between the neutron and proton potentials:

$$\begin{aligned} V_{\rm Lane}(\rho,p) &= \frac{V_{\rm n}-V_{\rm p}}{2\delta} \\ &= 2A_{\rm sym}\frac{\rho}{\rho_0} + 2B_{\rm sym}\left(\frac{\rho}{\rho_0}\right)^{\eta} \\ &\quad + \hbar^2 D_0\left(\frac{3\pi^2}{2}\rho\right)^{2/3}\rho + D_0\rho p^2 \\ &= V^{\rm loc}_{\rm sym} + 2D_0 m\rho E_k, \end{aligned} \tag{25}$$

where $V^{\rm loc}_{\rm sym} = 2A_{\rm sym}\frac{\rho}{\rho_0} + 2B_{\rm sym}(\frac{\rho}{\rho_0})^{\eta} + \hbar^2 D_0(\frac{3\pi^2}{2}\rho)^{2/3}\rho$ and $E_k = p^2/2m$.

To quantitatively understand the momentum and density dependence of $V_{\rm Lane}$ on HIC observables, we investigate $V_{\rm Lane}(\rho,p)$ for two typical Skyrme interaction parameter sets: SkM* and SLy4. These two Skyrme interaction parameter sets were selected for the following reasons: first, the incompressibility (K_0), symmetry energy coefficient (S_0), and isoscalar effective mass (m^*_s) should be within reasonable and commonly accepted ranges; that is, $K_0 = 230 \pm 20$ MeV, $S_0 = 32 \pm 2$ MeV, and $m^*_s/m = 0.7 \pm 0.1$. Second, the parameter sets have different signs of effective mass splitting: $\Delta m^*_{\rm np} = (m^*_{\rm n} - m^*_{\rm p})/m > 0$ or < 0. The SLy4 set [55] has $\Delta m^*_{\rm np} < 0$ (or $f_I > 0$) in neutron-rich matter, and the slope of the symmetry energy L is 46 MeV. The set SkM* has $\Delta m^*_{\rm np} > 0$ (or $f_I < 0$) and $L = 46$ MeV. For convenience, the values of the nuclear matter parameters in SkM* and SLy4 are listed in Table 2.

In Fig. 2, we present $V_{\rm Lane}$ as a function of kinetic energy for cold nuclear matter with isospin asymmetry $\delta = 0.2$ at different densities. $V_{\rm Lane}$ increased (decreased) as the kinetic energy increased for $\delta m^*_{\rm np} < 0$ ($\delta m^*_{\rm np} > 0$). They influence the neutron to proton yield ratio Y(n)/Y(p) as a function of the kinetic energy in HICs according to the following relationship:

$$\begin{aligned} \frac{Y(\rm n)}{Y(\rm p)} &\propto \exp\left(\frac{\mu_{\rm n}-\mu_{\rm p}}{T}\right) \\ &= \exp\left[\frac{2\left(V^{\rm loc}_{\rm sym} + 2D_0 m\rho E_{\rm k}\right)\delta}{T}\right], \end{aligned} \tag{26}$$

where T is the temperature of the emitting source and $\mu_{\rm n}$ and $\mu_{\rm p}$ are the chemical potentials of neutrons and protons, respectively. The above relationship can be obtained using statistical and dynamic models [56–61]. Therefore, one can expect that the larger the Lane potential, the larger the neutron to proton yield ratios. Similar effects on the triton to ^{3}He yield ratios are also expected [62]:

$$\begin{aligned} \frac{\rm Y(t)}{\rm Y(^3He)} &\propto \exp\left(\frac{\mu_{\rm t}-\mu_{^3\rm He}}{T}\right) \approx \exp\left(\frac{\mu_{\rm n}-\mu_{\rm p}}{T}\right) \\ &= \exp\left[\frac{2\left(V^{\rm loc}_{\rm sym} + 2D_0 m\rho E_k\right)\delta}{T}\right]. \end{aligned} \tag{27}$$

In addition, one can expect that the slopes of the Y(n)/Y(p) ratios with respect to E_k will differ from the effective mass splitting according to Eq. (26) and a similar behavior is also expected for Y(t)/Y(^{3}He).

3.3 *Y*(n)/*Y*(p) and *Y*(t)/*Y*(^{3}He)

To observe the effects of effective mass splitting on HIC observables such as Y(n)/Y(p) and Y(t)/Y(^{3}He), we performed a simulation of the ^{86}Kr + ^{208}Pb system at beam energies from $E_{\rm beam} = 25A$ to $200A$ MeV. In the calculations, the impact parameter $b = 1$ fm and the number of events were 100,000. The dynamic evolution time is stopped at 400 fm/c.

The left panels of Fig. 3 show the Y(n)/Y(p) ratios as functions of the normalized nucleon center-of-mass energy $E_{\rm k}/E_{\rm beam}$. The errors of Y(n)/Y(p) are statistical uncertainties obtained using the error propagation formula from the errors of Y(n) and Y(p). By using $E_{\rm k}/E_{\rm beam}$, the shapes of Y(n)/Y(p) as a function of the kinetic energy can be compared and understood on a similar scale for different beam energies. The red lines correspond to the results obtained with SLy4 ($m^*_{\rm n} < m^*_{\rm p}$) and the blue lines correspond to SkM* ($m^*_{\rm n} > m^*_{\rm p}$). Our calculations show that the Y(n)/Y(p) ratios obtained with

Table 1 Nuclear matter parameters calculated from 119 Skyrme interaction sets

Parameter	ρ_0	E_0	K_0	S_0	L	m_s^*	m_v^*
BSk9	0.159	− 15.90	231.56	30.00	39.90	0.80	0.91
BSk10	0.159	− 15.89	238.17	29.98	37.34	0.92	0.81
BSk11	0.159	− 15.84	239.03	30.04	38.34	0.92	0.82
BSk12	0.159	− 15.84	238.99	30.04	37.98	0.92	0.82
BSk13	0.159	− 15.84	239.02	30.04	38.81	0.92	0.82
BSk14	0.159	− 15.83	240.29	30.04	43.92	0.80	0.78
BSk15	0.159	− 16.02	241.70	30.00	33.62	0.80	0.77
BSk16	0.159	− 16.03	242.63	30.03	34.83	0.80	0.78
BSk17	0.159	− 16.03	242.65	30.03	36.25	0.80	0.78
FPLyon	0.162	− 15.90	217.20	30.94	42.78	0.84	0.97
Gs	0.158	− 15.57	238.13	31.46	94.32	0.78	0.68
KDE	0.164	− 15.97	223.13	31.93	41.44	0.76	0.86
KDE0v	0.161	− 16.08	229.01	32.99	45.22	0.72	0.77
KDE0v1	0.165	− 16.21	228.33	34.62	54.74	0.74	0.81
LNS	0.175	− 15.29	211.47	33.48	61.55	0.83	0.73
MSk1	0.157	− 15.81	232.62	29.96	34.05	1.00	1.00
MSL0	0.160	− 15.86	230.26	29.98	59.97	0.80	0.70
NRAPR	0.161	− 15.83	226.52	32.84	59.73	0.69	0.60
RATP	0.160	− 16.02	239.84	29.27	32.41	0.67	0.56
Rs	0.158	− 15.57	237.94	30.63	85.88	0.78	0.68
Sefm074	0.160	− 15.79	239.17	33.33	88.59	0.74	0.63
Sefm081	0.161	− 15.66	237.24	30.79	79.48	0.81	0.68
Sefm09	0.161	− 15.53	240.24	27.80	70.05	0.90	0.75
SGI	0.154	− 15.87	260.52	28.27	63.76	0.61	0.58
SGII	0.158	− 15.57	213.95	26.81	37.70	0.79	0.67
SKa	0.155	− 15.97	262.15	32.86	74.56	0.61	0.52
Ska25s20	0.161	− 16.05	221.45	33.83	63.90	0.98	0.98
SkI2	0.158	− 15.75	241.98	33.47	104.71	0.68	0.80
SkI4	0.160	− 15.92	247.64	29.48	60.36	0.65	0.80
SkI6	0.159	− 15.90	248.40	30.07	59.67	0.64	0.80
SkM	0.160	− 15.75	216.00	30.72	49.39	0.79	0.66
SkMs	0.160	− 15.75	216.00	30.01	45.84	0.79	0.65
SkMP	0.157	− 15.54	230.74	29.88	70.33	0.65	0.59
SkO	0.160	− 15.81	222.41	31.90	79.00	0.90	0.85
SkOp	0.160	− 15.73	221.94	31.92	68.92	0.90	0.87
SKRA	0.159	− 15.75	216.08	31.28	53.07	0.75	0.63
SkS1	0.161	− 15.84	227.93	28.74	30.65	0.86	0.64
SkSC14	0.161	− 15.90	235.96	30.02	33.11	1.00	1.00
SkT1	0.161	− 15.96	236.10	32.02	56.22	1.00	1.00
SkT1s	0.162	− 15.95	239.83	32.23	56.27	1.00	1.00
SkT1a	0.161	− 15.96	236.10	32.02	56.22	1.00	1.00
SkT2	0.161	− 15.92	235.66	32.00	56.20	1.00	1.00
SkT2a	0.161	− 15.92	235.66	32.00	56.20	1.00	1.00
SkT3	0.161	− 15.92	235.70	31.50	55.35	1.00	1.00
SkT3a	0.161	− 15.92	235.70	31.50	55.35	1.00	1.00
SkT6	0.161	− 15.94	236.21	29.97	30.85	1.00	1.00
SkT6a	0.161	− 15.94	236.21	29.97	30.85	1.00	1.00
SkT7	0.161	− 15.92	236.45	29.55	31.08	0.83	0.71
SkT7a	0.161	− 15.92	236.45	29.55	31.08	0.83	0.71
SkT8	0.161	− 15.92	236.40	29.94	33.69	0.83	0.83
SkT8a	0.161	− 15.92	236.40	29.94	33.69	0.83	0.83

Table 1 (continued)

Parameter	ρ_0	E_0	K_0	S_0	L	m_s^*	m_v^*
SkT9	0.160	– 15.86	234.22	29.73	33.82	0.83	0.83
SkT9a	0.160	– 15.86	234.22	29.73	33.82	0.83	0.83
SKX	0.155	– 16.03	269.76	31.07	33.40	0.99	0.75
SKXm	0.159	– 16.03	238.37	31.21	32.07	0.97	0.75
Skxs15	0.161	– 15.73	200.01	31.83	34.95	0.97	0.94
SLy0	0.160	– 15.95	229.00	31.95	47.10	0.70	0.80
SLy1	0.160	– 15.96	229.10	31.95	47.06	0.70	0.80
SLy2	0.161	– 15.96	230.86	32.04	47.49	0.70	0.80
Sly230b	0.160	– 15.95	230.84	32.04	45.99	0.69	0.80
SLy3	0.160	– 15.95	228.96	31.95	45.30	0.70	0.80
SLy4	0.160	– 15.95	230.84	32.04	45.96	0.69	0.80
SLy5	0.161	– 15.96	230.77	32.05	48.18	0.70	0.80
SLy6	0.159	– 15.90	229.91	31.95	47.45	0.69	0.80
SLy7	0.158	– 15.88	228.98	31.95	46.93	0.69	0.80
SLy8	0.160	– 15.95	229.18	31.96	47.16	0.70	0.80
SLy9	0.151	– 15.77	229.41	31.95	54.82	0.67	0.80
SLy10	0.156	– 15.88	230.56	32.01	38.72	0.68	0.80
QMC600	0.174	– 16.40	221.21	34.65	46.81	0.81	0.61
QMC650	0.172	– 16.21	221.48	33.88	53.38	0.78	0.63
QMC700	0.171	– 16.11	223.89	33.69	59.49	0.76	0.64
QMC750	0.171	– 16.21	225.98	33.96	65.10	0.74	0.65
SV-bas	0.160	– 15.88	234.23	30.03	32.33	0.90	0.71
SV-K218	0.161	– 15.88	217.32	29.97	34.78	0.90	0.72
SV-K226	0.160	– 15.88	224.80	29.97	34.27	0.90	0.72
SV-K241	0.159	– 15.89	241.55	30.02	30.94	0.90	0.71
SV-kap20	0.160	– 15.88	234.08	30.03	35.52	0.90	0.83
SV-mas07	0.160	– 15.87	233.76	30.01	52.18	0.70	0.71
SV-mas08	0.160	– 15.88	233.64	30.02	40.17	0.80	0.71
SV-min	0.161	– 15.89	221.55	30.65	44.85	0.95	0.93
SV-sym32	0.159	– 15.92	232.74	31.95	57.11	0.90	0.72
SV-sym34	0.159	– 15.94	233.50	33.96	80.92	0.90	0.72
SV-tls	0.160	– 15.87	234.32	30.04	33.16	0.90	0.71
T11	0.161	– 15.99	229.46	31.97	49.45	0.70	0.80
T12	0.161	– 15.98	229.73	31.98	49.37	0.70	0.80
T13	0.161	– 15.98	229.83	31.99	49.53	0.70	0.80
T14	0.161	– 15.97	229.79	31.98	49.47	0.70	0.80
T15	0.161	– 15.98	229.48	31.97	49.63	0.70	0.80
T16	0.161	– 15.99	229.71	31.98	49.44	0.70	0.80
T21	0.161	– 16.00	228.97	31.94	49.74	0.70	0.80
T22	0.161	– 16.00	229.18	31.95	49.54	0.70	0.80
T23	0.161	– 15.99	229.35	31.96	49.57	0.70	0.80
T24	0.161	– 15.99	229.52	31.97	49.84	0.70	0.80
T25	0.161	– 15.97	230.24	32.01	49.14	0.70	0.80
T26	0.161	– 15.95	230.33	32.01	48.77	0.70	0.80
T31	0.161	– 16.00	229.32	31.96	49.73	0.70	0.80
T32	0.161	– 16.00	229.06	31.95	50.25	0.70	0.80
T33	0.161	– 16.00	229.47	31.97	49.64	0.70	0.80
T34	0.161	– 16.00	229.05	31.95	50.06	0.70	0.80
T35	0.161	– 15.98	230.12	32.00	49.60	0.70	0.80
T36	0.161	– 15.97	229.66	31.98	49.05	0.70	0.80
T41	0.162	– 16.04	230.24	32.01	50.62	0.71	0.80

Table 1 (continued)

Parameter	ρ_0	E_0	K_0	S_0	L	m_s^*	m_v^*
T42	0.162	– 16.03	230.55	32.02	50.74	0.70	0.80
T43	0.162	– 16.02	230.88	32.04	50.62	0.70	0.80
T44	0.161	– 16.00	229.47	31.97	50.04	0.70	0.80
T45	0.161	– 16.00	229.14	31.95	49.63	0.70	0.80
T46	0.161	– 15.98	230.46	32.02	49.96	0.70	0.80
T51	0.162	– 16.03	230.73	32.03	50.73	0.70	0.80
T52	0.161	– 16.03	228.94	31.94	50.64	0.70	0.80
T53	0.161	– 16.00	229.40	31.97	50.01	0.70	0.80
T54	0.161	– 16.01	229.26	31.96	50.25	0.70	0.80
T55	0.161	– 16.01	228.95	31.94	50.20	0.70	0.80
T56	0.161	– 15.99	229.87	31.99	50.13	0.70	0.80
T61	0.162	– 16.05	230.27	32.01	50.81	0.71	0.80
T62	0.162	– 16.05	230.17	32.00	50.34	0.71	0.80
T63	0.162	– 16.04	230.34	32.01	51.09	0.70	0.80
T64	0.162	– 16.01	231.00	32.04	50.54	0.70	0.80
T65	0.162	– 16.02	230.73	32.03	50.54	0.70	0.80
T66	0.161	– 16.00	229.28	31.96	50.28	0.70	0.80

Table 2 Nuclear matter parameters of SLy4 and SkM*

Parameter	ρ_0	E_0	K_0	S_0	L	m_s^*/m	m_v^*/m
SLy4	0.160	– 15.97	230	32	46	0.69	0.80
SkM*	0.160	– 15.77	217	30	46	0.79	0.65

The parameters E_0, K_0, S_0, and L are in MeV, and ρ_0 is in fm^{-3}

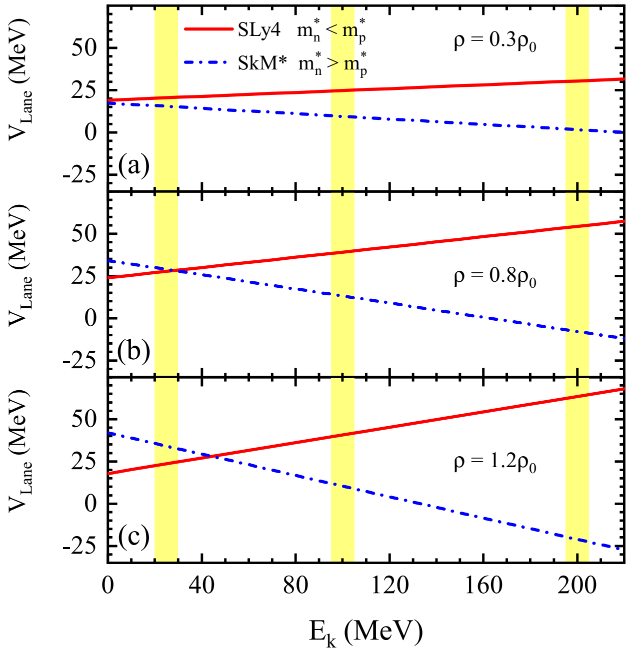

Fig. 2 (Color online) Lane potential V_{Lane} as functions of kinetic energy E_{k} at densities of $\rho = 0.3\rho_0$, $0.8\rho_0$, and $1.2\rho_0$

both SLy4 and SkM* decrease as the nucleon kinetic energy increases, owing to Coulomb effects. Furthermore, the $Y(\mathrm{n})/Y(\mathrm{p})$ ratios obtained using SLy4 ($m_{\mathrm{n}}^* < m_{\mathrm{p}}^*$) are larger than those obtained using SkM* ($m_{\mathrm{n}}^* > m_{\mathrm{p}}^*$). At a beam energy of 200*A* MeV, a flatter $Y(\mathrm{n})/Y(\mathrm{p})$ dependence on the nucleon kinetic energy was observed for SLy4. This is because SLy4 has stronger Lane potentials at high kinetic energies and enhanced neutron emission at high nucleon energies.

Specifically, the difference in $Y(\mathrm{n})/Y(\mathrm{p})$ between SLy4 ($m_{\mathrm{n}}^* < m_{\mathrm{p}}^*$) and SkM*($m_{\mathrm{n}}^* > m_{\mathrm{p}}^*$) maintains a constant value with the nucleon kinetic energy at 25*A* MeV and increases with the nucleon kinetic energy at a beam energy of > 100*A* MeV. This can be understood from the Lane potentials shown in Fig. 2. At 25*A* MeV, the system is less compressed and excited than that at 100*A* or 200*A* MeV, and most of the emitted nucleons originate from the low-density region. The corresponding symmetry potentials for SLy4 and SkM* varied weakly as a function of kinetic energy (see Fig. 2a). Therefore, one can expect that the difference in $Y(\mathrm{n})/Y(\mathrm{p})$ between SLy4 ($m_{\mathrm{n}}^* < m_{\mathrm{p}}^*$) and SkM* ($m_{\mathrm{n}}^* > m_{\mathrm{p}}^*$) is small and changes weakly as the kinetic energy increases. At a beam

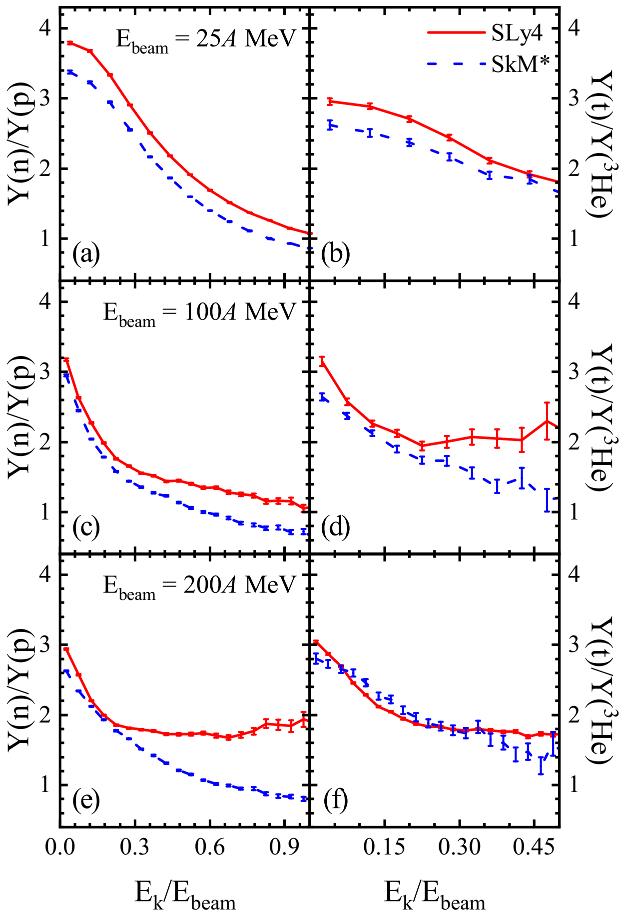

Fig. 3 (Color online) Yield ratios of Y(n)/Y(p) and Y(t)/Y(^{3}He) as functions of the normalized nucleon center-of-mass energy E_k/E_{beam} at beam energies of E_{beam} = 25A, 100A, and 200A MeV

Table 3 Coefficients of determination, R^2, for the linear fit of ln(Y(n)/Y(p)) and ln(Y(t)/Y(^{3}He))

R^2	ln(Y(n)/Y(p))		ln(Y(t)/Y(^{3}He))	
	SLy4	SkM*	SLy4	SkM*
25A MeV	0.98767	0.98431	0.99073	0.97503
100A MeV	0.97342	0.98295	0.50164	0.84234
200A MeV	0.36945	0.96828	0.79116	0.66351

energy of > 100A MeV, the system can be compressed to higher densities, where the magnitude of the splitting increases with the kinetic energy, as shown in Fig. 2b, c.

The right panels of Fig. 3 show the Y(t)/Y(^{3}He) ratios as functions of the normalized nucleon center-of-mass energy, that is, E_k/E_{beam}. Similar to Y(n)/Y(p), the Y(t)/Y(^{3}He) ratios are also sensitive to effective mass splitting. This can also be explained using Eq. (27). At a beam energy of 200A MeV, the sensitivity of the Y(t)/Y(^{3}He) ratios to the kinetic energy becomes weak, which may be due to cluster effects and stronger nonequilibrium effects than those at lower beam energies.

Furthermore, Fig. 3 also shows that the Y(n)/Y(p) ratio decreases exponentially with respect to E_k/E_{beam} in the range $0.3 \leqslant E_k/E_{beam} \leqslant 1.0$. For t/^{3}He ratios, a similar behavior can be observed in $0.2 \leqslant E_k/E_{beam} \leqslant 0.5$ since the kinetic energy per nucleon for the emitted tritons or ^{3}He is approximately one-half of the beam energy. According to Eqs. (26) and (27), the exponentially decreasing behavior indicates that the emitted nucleons are in equilibrium in momentum space and can be described by the slopes of ln[Y(n)/Y(p)] or ln[Y(t)/Y(^{3}He)], and the slopes of ln[Y(n)/Y(p)] and ln[Y(t)/Y(^{3}He)] are directly related to D_0 as follows:

$$S_{n/p} = \frac{\partial \ln[Y(n)/Y(p)]}{\partial E_k} = 4D_0 m\delta\rho/T, \qquad (28)$$
$$S_{t/^3He} = \frac{\partial \ln[Y(t)/Y(^3He)]}{\partial E_k} = 4D_0 m\delta\rho/T.$$

In the following analysis, we perform the linear fit of ln[Y(n)/Y(p)] and ln[Y(t)/Y(^{3}He)]:

$$\ln\left[\frac{Y(n)}{Y(p)}\right] = S_{n/p}\frac{E_k}{E_{beam}} + b_0^{n/p} \qquad (29)$$

in the range of $0.3 \leqslant E_k/E_{beam} \leqslant 1.0$ and

$$\ln\left[\frac{Y(t)}{Y(^3He)}\right] = S_{t/^3He}\frac{E_k}{E_{beam}} + b_0^{t}/^3He \qquad (30)$$

in the range of $0.2 \leqslant E_k/E_{beam} \leqslant 0.5$ to obtain the slopes of $S_{n/p}$ ($S_{t/^3He}$) and the intercepts of $b_0^{n/p}$ ($b_0^{t/^3He}$). To describe the goodness of linear fit of ln(Y(n)/Y(p)) and ln(Y(t)/Y(^{3}He)), we present the coefficients of determination, R^2 [63] in Table 3.

Figure 4 presents $S_{n/p}$ ($S_{t/^3He}$) and $b_0^{n/p}$ ($b_0^{t/^3He}$) as functions of the beam energy to determine the optimal energy for probing effective mass splitting. Panel (a) shows $S_{n/p}$ and panel (c) shows $S_{t/^3He}$. Our calculations show that the values of $S_{n/p}$ ($S_{t/^3He}$) obtained with SLy4 are higher than those obtained with SkM* except for the beam energy of 25A MeV. Specifically, the impact of effective mass splitting on $S_{n/p}$ becomes evident at a beam energy of 200A MeV. For $S_{t/^3He}$, the impact of effective mass splitting is greatest at a beam energy of ~ 100A MeV under the influence of the cluster formation mechanism. For the $b_0^{n/p}$, the calculations show that it weakly depends on the effective mass splitting, except for the value of $b_0^{n/p}$ at beam energies E_{beam} = 200A MeV. At this beam energy, the value of $b_0^{n/p}$ obtained using SkM* is larger than that obtained using SLy4. For $b_0^{t/^3He}$, the value obtained using SkM* was lower than that obtained using SLy4 at a beam energy of 25A MeV. At E_{beam} > 100A MeV, the values of $b_0^{t/^3He}$ obtained with SkM* were greater than those obtained with SLy4.

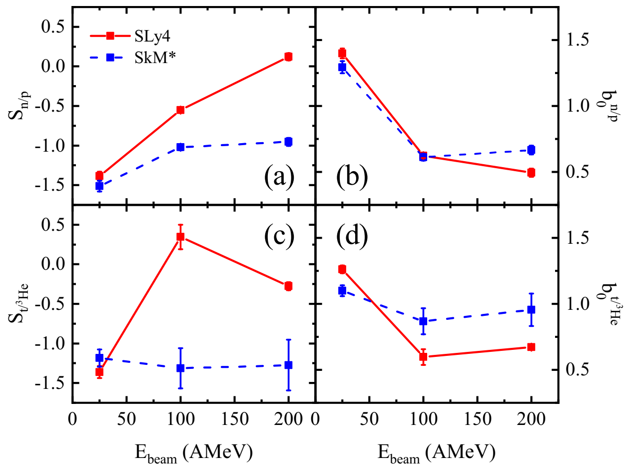

Fig. 4 (Color online) S_X and b_0^X as functions of E_{beam} for SLy4 and SkM*. Upper panels are X = n/p and bottom panels are X = t/^{3}He

4 Summary and outlook

In summary, we compiled 119 Skyrme interaction sets and their corresponding nuclear matter parameters to understand the correlations between different nuclear matter parameters. By analyzing the linear correlation coefficient, the strength of the correlation between different nuclear matter parameters was quantitatively obtained. Furthermore, the correlations between different nuclear parameters indicates that obtaining tight constraints on the symmetry energy requires knowing not only the values of the symmetry energy coefficient S_0 and the slope of the symmetry energy L but the isoscalar effective mass m_s^* and the isovector effective mass m_v^* or the effective mass splitting, given that K_0 and E_0 are well constrained.

To understand the impact of effective mass splitting on HIC observables, we simulated the ^{86}Kr + ^{208}Pb system at beam energies ranging from 25 to 200 MeV per nucleon. Two observables were analyzed: the emitted neutron to proton yield ratio and the triton to ^{3}He yield ratio. Our results show that the energy spectra of Y(n)/Y(p) and Y(t)/Y(^{3}He) can be used to distinguish the effective mass splitting, which is consistent with previous studies in Refs. [13, 45]. Furthermore, we constructed the characteristic variables, namely the slope and intercept of ln[Y(n)/Y(p)] and ln[Y(t)/Y(^{3}He)], respectively, which can be directly related to the effective mass splitting. The greatest effects were observed at 200A MeV for (Y(n)/Y(p)), whereas the greatest effects were observed at 100A MeV for (Y(t)/Y(^{3}He)). This difference can be attributed to the cluster formation mechanism.

Appendix 1: Single-particle potential

For the Skyrme interaction, the single-particle potential in uniform nuclear matter can be written as the summation of the local and nonlocal (momentum-dependent) parts as follows:

$$V_q = V_q^{\mathrm{loc}} + V_q^{\mathrm{md}}. \tag{A.1}$$

Based on the definition of the single-particle potential, V_q should be obtained from the derivatives of the net energy E of the system with respect to the number of particles. For the local part, V_q^{loc} is

$$\begin{aligned} V_q^{\mathrm{loc}}(\rho,\delta) &= \frac{\partial u_{\mathrm{loc}}(\rho,\delta)}{\partial \rho_q} \\ &= \alpha\frac{\rho}{\rho_0} + \beta\frac{\rho^\eta}{\rho_0^\eta} + (\eta-1)B_{\mathrm{sym}}\frac{\rho^\eta}{\rho_0^\eta}\delta^2 \\ &\quad \pm 2\left(A_{\mathrm{sym}}\frac{\rho}{\rho_0} + B_{\mathrm{sym}}\left(\frac{\rho}{\rho_0}\right)^\eta\right)\delta, \end{aligned} \tag{A.2}$$

where '+' is for neutrons and '−' for protons. The nonlocal part of the single-particle potential depends not only on the position but also on the momentum, which can be obtained by taking the functional derivative of the energy density with respect to the phase-space distribution function of protons or neutrons $f_q(r,p)$:

$$\begin{aligned} V_q^{\mathrm{md}}(\rho,\delta,p) &= \frac{\delta u_{\mathrm{md}}}{\delta f_q} \\ &= 2(C_0\rho + D_0\rho_q)p^2 + 2\hbar^2 C_0\tau + 2\hbar^2 D_0\tau_q, \end{aligned} \tag{A.3}$$

where τ is the kinetic energy density and is the summation of the kinetic energy densities of neutrons and protons (i.e.,$\tau = \tau_{\mathrm{n}} + \tau_{\mathrm{p}}$) and $\tau_q = \frac{3}{5}k_{q,F}^2\rho_q$, with $k_{q,F} = (3\pi^2\rho_q)^{1/3}$.

Author contributions All authors contributed to the study conception and design. Material preparation, data collection, and analysis were performed by Fang-Yuan Wang, Jun-Ping Yang, Xiang Chen, Ying Cui, Yong-Jia Wang, Zhi-Gang Xiao, Zhu-Xia Li, and Ying-Xun Zhang. The first draft of the manuscript was written by Fang-Yuan Wang and Ying-Xun Zhang and all authors commented on previous versions of the manuscript. All authors read and approved the final manuscript.

References

1. B.A. Li, B.J. Cai, L.W. Chen et al., Nucleon effective masses in neutron-rich matter. Prog. Part. Nucl. Phys. **99**, 29–119 (2018). https://doi.org/10.1016/j.ppnp.2018.01.001
2. J. Jeukenne, A. Lejeune, C. Mahaux, Many-body theory of nuclear matter. Phys. Rep. **25**, 83–174 (1976). https://doi.org/10.1016/0370-1573(76)90017-X

3. X.L. Shang, A. Li, Z.Q. Miao et al., Nucleon effective mass in hot dense matter. Phys. Rev. C **101**, 065801 (2020). https://doi.org/10.1103/PhysRevC.101.065801
4. A. Li, J.N. Hu, X.L. Shang et al., Nonrelativistic nucleon effective masses in nuclear matter: Brueckner–hartree–fock model versus relativistic hartree–fock model. Phys. Rev. C **93**, 015803 (2016). https://doi.org/10.1103/PhysRevC.93.015803
5. P.S. Shternin, Transport coefficients of leptons in superconducting neutron star cores. Phys. Rev. D **98**, 063015 (2018). https://doi.org/10.1103/PhysRevD.98.063015
6. A.Y. Potekhin, A.I. Chugunov, G. Chabrier, Thermal evolution and quiescent emission of transiently accreting neutron stars. Astron. Astrophys. **629**, 16 (2019). https://doi.org/10.1051/0004-6361/201936003
7. M. Baldo, G.F. Burgio, Properties of the nuclear medium. Rep. Progr. Phys. **75**, 026301 (2012). https://doi.org/10.1088/0034-4885/75/2/026301
8. D. Page, J.M. Lattimer, M. Prakash et al., Minimal cooling of neutron stars: a new paradigm. Astrophys. J. Suppl. Ser. **155**, 623 (2004). https://doi.org/10.1086/424844
9. A. Dehghan Niri, H.R. Moshfegh, P. Haensel, Nuclear correlations and neutrino emissivity from the neutron branch of the modified urca process. Phys. Rev. C **93**, 045806 (2016). https://doi.org/10.1103/PhysRevC.93.045806
10. A. Dehghan Niri, H.R. Moshfegh, P. Haensel, Role of nuclear correlations and kinematic effects on neutrino emission from the modified urca processes. Phys. Rev. C **98**, 025803 (2018). https://doi.org/10.1103/PhysRevC.98.025803
11. P.S. Shternin, M. Baldo, P. Haensel, In-medium enhancement of the modified urca neutrino reaction rates. Phys. Lett. B **786**, 28–34 (2018). https://doi.org/10.1016/j.physletb.2018.09.035
12. J.B. Wei, G.F. Burgio, H.J. Schulze, Neutron star cooling with microscopic equations of state. Month. Not. R. Astron. Soc. **484**, 5162–5169 (2019). https://doi.org/10.1093/mnras/stz336
13. Y. Zhang, M. Tsang, Z. Li et al., Constraints on nucleon effective mass splitting with heavy ion collisions. Phys. Lett. B **732**, 186–190 (2014). https://doi.org/10.1016/j.physletb.2014.03.030
14. D.D.S. Coupland, M. Youngs, Z. Chajecki et al., Probing effective nucleon masses with heavy-ion collisions. Phys. Rev. C **94**, 011601 (2016). https://doi.org/10.1103/PhysRevC.94.011601
15. Z.Q. Feng, Effective mass splitting of neutron and proton and isospin emission in heavy-ion collisions. Nucl. Phys. A **878**, 3–13 (2012). https://doi.org/10.1016/j.nuclphysa.2012.01.014
16. W.J. Xie, J. Su, L. Zhu et al., Neutron-proton effective mass splitting in a Boltzmann–Langevin approach. Phys. Rev. C **88**, 061601 (2013). https://doi.org/10.1103/PhysRevC.88.061601
17. J. Su, L. Zhu, C.Y. Huang et al., Effects of symmetry energy and effective k-mass splitting on central ^{96}Ru(^{96}Zr) + ^{96}Zr(^{96}Ru) collisions at 50 to 400 mev/nucleon. Phys. Rev. C **96**, 024601 (2017). https://doi.org/10.1103/PhysRevC.96.024601
18. G.F. Wei, Q.J. Zhi, X.W. Cao et al., Examination of an isospin-dependent single-nucleon momentum distribution for isospin-asymmetric nuclear matter in heavy-ion collisions. Nucl. Scie. Tech. **31**, 71 (2020). https://doi.org/10.1007/s41365-020-00779-6
19. B.A. Li, Constraining the neutron-proton effective mass splitting in neutron-rich matter. Phys. Rev. C **69**, 064602 (2004). https://doi.org/10.1103/PhysRevC.69.064602
20. X.H. Li, W.J. Guo, B.A. Li et al., Neutron-proton effective mass splitting in neutron-rich matter at normal density from analyzing nucleon-nucleus scattering data within an isospin dependent optical model. Phys. Lett. B **743**, 408–414 (2015). https://doi.org/10.1016/j.physletb.2015.03.005
21. C. Xu, B.A. Li, L.W. Chen, Symmetry energy, its density slope, and neutron-proton effective mass splitting at normal density extracted from global nucleon optical potentials. Phys. Rev. C **82**, 054607 (2010). https://doi.org/10.1103/PhysRevC.82.054607
22. Z. Zhang, L.W. Chen, Isospin splitting of the nucleon effective mass from giant resonances in ^{208}Pb. Phys. Rev. C **93**, 034335 (2016). https://doi.org/10.1103/PhysRevC.93.034335
23. H.Y. Kong, J. Xu, L.W. Chen et al., Constraining simultaneously nuclear symmetry energy and neutron-proton effective mass splitting with nucleus giant resonances using a dynamical approach. Phys. Rev. C **95**, 034324 (2017). https://doi.org/10.1103/PhysRevC.95.034324
24. J. Su, L. Zhu, C. Guo, Constraints on the effective mass splitting by the isoscalar giant quadrupole resonance. Phys. Rev. C **101**, 044606 (2020). https://doi.org/10.1103/PhysRevC.101.044606
25. J. Xu, W.T. Qin, Nucleus giant resonances from an improved isospin-dependent Boltzmann–Uehling–Uhlenbeck transport approach. Phys. Rev. C **102**, 024306 (2020). https://doi.org/10.1103/PhysRevC.102.024306
26. P. Morfouace, C. Tsang, Y. Zhang et al., Constraining the symmetry energy with heavy-ion collisions and Bayesian analyses. Phys. Lett. B **799**, 135045 (2019). https://doi.org/10.1016/j.physletb.2019.135045
27. X.H. Zhou, Physics opportunities at the new facility hiaf. Nucl. Phys. Rev. **35**, 339 (2018). https://doi.org/10.11804/NuclPhysRev.35.04.339
28. P.N. Ostroumov, S. Cogan, K. Fukushima et al., Heavy ion beam acceleration in the first three cryomodules at the facility for rare isotope beams at Michigan state university. Phys. Rev. Accel. Beams **22**, 040101 (2019). https://doi.org/10.1103/PhysRevAccelBeams.22.040101
29. H. Sakurai, Ri beam factory project at Riken. Nucl. Phys. A **805**, 526c–532c (2008). https://doi.org/10.1016/j.nuclphysa.2008.02.291
30. B. Hong, Y. Go, G. Jhang et al., Plan for nuclear symmetry energy experiments using the lamps system at the rib facility Raon in Korea. Eur. Phys. J. A **50**, 11 (2014). https://doi.org/10.1140/epja/i2014-14049-2
31. W.P. Liu, The prospects for accelerator-based nuclear physics facilities. Physics **43**, 150 (2014). https://doi.org/10.7693/wl20140301
32. Y. Zhang, M. Tsang, Z. Li et al., Constraints on nucleon effective mass splitting with heavy ion collisions. Phys. Lett. B **732**, 186–190 (2014). https://doi.org/10.1016/j.physletb.2014.03.030
33. M. Mocko, M.B. Tsang, Z.Y. Sun et al., Projectile fragmentation of ^{86}Kr at 64 mev/nucleon. Phys. Rev. C **76**, 014609 (2007). https://doi.org/10.1103/PhysRevC.76.014609
34. M.B. Tsang, Y. Zhang, P. Danielewicz et al., Constraints on the density dependence of the symmetry energy. Phys. Rev. Lett. **102**, 122701 (2009). https://doi.org/10.1103/PhysRevLett.102.122701
35. J. Estee, Charged pion emission from neutron-rich heavy ion collisions for studies on the symmetry energy. Ph.D. thesis 188 (2020).https://doi.org/10.25335/s6mp-5668
36. L. Li, F.Y. Wang, Y.X. Zhang, Isospin effects on intermediate mass fragments at intermediate energy-heavy ion collisions. Nucl. Scie. Tech. **33**, 58 (2022). https://doi.org/10.1007/s41365-022-01050-w
37. L.W. Chen, C.M. Ko, B.A. Li, Determination of the stiffness of the nuclear symmetry energy from isospin diffusion. Phys. Rev. Lett. **94**, 032701 (2005). https://doi.org/10.1103/PhysRevLett.94.032701
38. F. Guan, X. Diao, Y. Wang et al., A compact spectrometer for heavy ion experiments in the fermi energy regime. Nucl. Instrum. Methods Phys. Res. Sect. A: Accel. Spectrom. Detect. Assoc. Equip. **1011**, 165592 (2021). https://doi.org/10.1016/j.nima.2021.165592
39. Y.J. Wang, F.H. Guan, X.Y. Diao et al., Cshine for studies of hbt correlation in heavy ion reactions. Nucl. Sci. Tech. **32**, 4 (2021). https://doi.org/10.1007/s41365-020-00842-2

40. Y. Wang, F. Guan, X. Diao et al., Observing the ping-pong modality of the isospin degree of freedom in cluster emission from heavy-ion reactions. Phys. Rev. C **107**, L041601 (2023). https://doi.org/10.1103/PhysRevC.107.L041601
41. X.Y. Diao, F.H. Guan, Y.J. Wang et al., Reconstruction of fission events in heavy ion reactions with the compact spectrometer for heavy ion experiment. Nucl. Scie. Tech. **33**, 40 (2022). https://doi.org/10.1007/s41365-022-01024-y
42. Z. Sun, W.L. Zhan, Z.Y. Guo et al., RIBLL, the radioactive ion beam line in Lanzhou. Nucl. Instrum. Meth. Phys. Res. Sect. A **503**, 496–503 (2003). https://doi.org/10.1016/S0168-9002(03)01005-2
43. H.L. Wang, Z. Wang, C.S. Gao et al., Design and tests of the prototype beam monitor of the csr external target experiment. Nucl. Sci. Tech. **33**, 36 (2022)
44. Y. Zhang, Z. Li, Probing the density dependence of the symmetry potential with peripheral heavy-ion collisions. Phys. Rev. C **71**, 024604 (2005). https://doi.org/10.1103/PhysRevC.71.024604
45. J. Rizzo, M. Colonna, M. Di Toro et al., Transport properties of isospin effective mass splitting. Nucl. Phys. A **732**, 202–217 (2004). https://doi.org/10.1016/j.nuclphysa.2003.11.057
46. Y. Zhang, N. Wang, Q.F. Li et al., Progress of quantum molecular dynamics model and its applications in heavy ion collisions. Front. Phys. **15**, 54301 (2020). https://doi.org/10.1007/s11467-020-0961-9
47. T.H.R. Skyrme, CVII. The nuclear surface. Philos. Mag. J. Theor. Exp. Appl. Phys. **1**, 1043–1054 (1956). https://doi.org/10.1080/14786435608238186
48. J. Yang, Y. Zhang, N. Wang et al., Influence of the treatment of initialization and mean-field potential on the neutron to proton yield ratios. Phys. Rev. C **104**, 024605 (2021). https://doi.org/10.1103/PhysRevC.104.024605
49. Y. Zhang, Z. Li, Elliptic flow and system size dependence of transition energies at intermediate energies. Phys. Rev. C **74**, 014602 (2006). https://doi.org/10.1103/PhysRevC.74.014602
50. Y. Zhang, M. Liu, C.J. Xia et al., Constraints on the symmetry energy and its associated parameters from nuclei to neutron stars. Phys. Rev. C **101**, 034303 (2020). https://doi.org/10.1103/PhysRevC.101.034303
51. F. Zhang, J. Su, Probing neutron-proton effective mass splitting using nuclear stopping and isospin mix in heavy-ion collisions in gev energy region. Nucl. Scie. Tech. **31**, 77 (2020). https://doi.org/10.1007/s41365-020-00787-6
52. H. Wolter, M. Colonna, D. Cozma et al., Transport model comparison studies of intermediate-energy heavy-ion collisions. Prog. Part. Nucl. Phys. **125**, 103962 (2022). https://doi.org/10.1016/j.ppnp.2022.103962
53. J. Xu et al., Understanding transport simulations of heavy-ion collisions at 100A and 400A MeV: comparison of heavy-ion transport codes under controlled conditions. Phys. Rev. C **93**, 044609 (2016). https://doi.org/10.1103/PhysRevC.93.044609
54. Y. Zhang, Z. Li, Elliptic flow and system size dependence of transition energies at intermediate energies. Phys. Rev. C **74**, 014602 (2006). https://doi.org/10.1103/PhysRevC.74.014602
55. E. Chabanat, P. Bonche, P. Haensel et al., A skyrme parametrization from subnuclear to neutron star densities. Nucl. Phys. A **627**, 710–746 (1997). https://doi.org/10.1016/S0375-9474(97)00596-4
56. M.B. Tsang, W.A. Friedman, C.K. Gelbke et al., Isotopic scaling in nuclear reactions. Phys. Rev. Lett. **86**, 5023–5026 (2001). https://doi.org/10.1103/PhysRevLett.86.5023
57. M.B. Tsang, C.K. Gelbke, X.D. Liu et al., Isoscaling in statistical models. Phys. Rev. C **64**, 054615 (2001). https://doi.org/10.1103/PhysRevC.64.054615
58. A. Ono, P. Danielewicz, W.A. Friedman et al., Isospin fractionation and isoscaling in dynamical simulations of nuclear collisions. Phys. Rev. C **68**, 051601 (2003). https://doi.org/10.1103/PhysRevC.68.051601
59. S. Das Gupta, A. Mekjian, The thermodynamic model for relativistic heavy ion collisions. Phys. Rep. **72**, 131–183 (1981). https://doi.org/10.1016/0370-1573(81)90012-0
60. G. Fai, A.Z. Mekjian, Minimal information and statistical descriptions of nuclear fragmentation. Phys. Lett. B **196**, 281–284 (1987). https://doi.org/10.1016/0370-2693(87)90731-3
61. A.S. Botvina, O.V. Lozhkin, W. Trautmann, Isoscaling in light-ion induced reactions and its statistical interpretation. Phys. Rev. C **65**, 044610 (2002). https://doi.org/10.1103/PhysRevC.65.044610
62. Z. Chajecki, M. Youngs, D.D.S. Coupland, et al., Scaling properties of light-cluster production. (2014). arXiv:1402.5216
63. A. Di Bucchianico, *Coefficient of Determination (R2)* (Wiley, 2008). https://doi.org/10.1002/9780470061572.eqr173

Springer Nature or its licensor (e.g. a society or other partner) holds exclusive rights to this article under a publishing agreement with the author(s) or other rightsholder(s); author self-archiving of the accepted manuscript version of this article is solely governed by the terms of such publishing agreement and applicable law.